



LAWRENCE  
LIVERMORE  
NATIONAL  
LABORATORY

# Tensile and microstructural properties of low-temperature neutron irradiated base metal and electron-beam welded 316L type stainless steel

C. M. Silva, K. J. Leonard, L. M. Garrison, C. D. Bryan, K. S. Holliday

July 14, 2021

Metall Mater Trans A (2022)



33 2. Introduction

34 There are different grades of 316 austenite stainless steels (SS) of which 316, 316L, 316LN, and  
35 316H are well known due to their different properties and use in industry. The elemental composition of  
36 these austenite steels varies depending on the product, and the presence of Cr, Ni, and Mo brings  
37 favorable properties to the material. The C levels of the austenite SS are of note due to its impact on  
38 mechanical and chemical properties of the austenite steels, especially at high temperatures. The low C  
39 levels also reduce the effects of sensitization at moderate temperatures (<500 °C) that usually promote the  
40 precipitation of carbides at grain boundaries affecting the properties of SS deleteriously.<sup>1</sup> Usually, 0.01–  
41 0.03, 0.03–0.08, and 0.04–0.10% C levels can be found in 316L, 316, and 316H, respectively. In 316LN,  
42 the C levels will be comparable to 316L but with larger N content (0.12–0.22%, whereas it is ~0.11% in  
43 316L).

44 These austenite steels have good formability and possess high creep, considerably high ductility, and  
45 tensile strength even at high temperatures. Type 316 steels also have higher resistance to general and  
46 pitting corrosion than type 304. As a result of these favorable properties, type 316 SS has been used as a  
47 structural material in nuclear power industry, especially for the internal structure components in light  
48 water reactors (LWRs) or pressurized water reactors (PWRs).<sup>2</sup> Austenite SS has also been considered in  
49 a number of other nuclear applications. For example, in fast breeder reactors (FBR) such as liquid metal  
50 cooled fast breeder reactors (LMFBR), fusion reactors: next European torus (NET) fusion program and  
51 international thermonuclear experimental reactor (ITER), as a mercury target vessel for spallation neutron  
52 source (SNS), and etc.<sup>3, 4, 5, 6, 7, 8, 9, 10, 11</sup>

53 While there is a considerable amount of reported research in the literature on neutron irradiation study  
54 of type 316 SS, low-temperature irradiation studies are scarce. Among few of those studies, Saito has  
55 carried out a neutron irradiation experiment on 316L base metal (BSM) and welded joints at 180–200 °C  
56 with fast neutron fluences of  $1.2\text{--}3.4 \times 10^{22}$  n/m<sup>2</sup> (E>1 MeV).<sup>7</sup> Elen also has conducted a fast neutron  
57 irradiation study of austenite steels including 316L at a comparatively low 250 °C temperature, where  
58 they mainly focused on radiation hardening of austenite steels subjected to different processing  
59 conditions.<sup>12</sup> Another neutron irradiation study was carried out on 316L(N) SS in base metal and  
60 electron-beam (e-beam) welded states at 227, 327, and 427 °C temperatures.<sup>5</sup> These studies have shown  
61 that irradiation increases 316 type steels tensile strengths and decrease the ductility in a closely similar  
62 manner. While irradiation hardening of 316 austenite steels was also reported, its level sometimes is a  
63 variant of the different irradiation temperatures regardless of the effects of other properties such as grain  
64 size and/or processing conditions such as cold working.

65 There has also been recent interest in using 316L as a structural material for a small-scale nuclear  
66 vessel that is designed for the domestic production of Mo-99.<sup>13</sup> This vessel will contain some structural

67 parts which will be exposed to neutron irradiation at lower temperatures, with excursions under abnormal  
 68 operating conditions self-limiting to less than 100 °C, than the light water reactors currently operating in  
 69 the US. Since the mechanical properties of SS 316L at such low temperatures are scarce to find in the  
 70 literature, the current study has been focused on collecting and studying mechanical properties, especially  
 71 tensile type, for 316L samples under its base metal and electron-beam welded forms. The tensile behavior  
 72 of the samples is further discussed with complementary microscopic characterization (optical and  
 73 scanning electron).

### 75 3. Experimental details

#### 76 3.1 Materials

77 The stainless steel 316L grade alloys used in this research were purchased through Metal Suppliers.  
 78 Acciaierie Valbruna produced the 316L stainless steel (heat 251393 and lot number 105700560) through  
 79 rolling to a 0.75 in. (19.05 mm) thick product form and annealing at 1060 °C for 1 h, followed by water  
 80 quenching. The chemical composition of the 316L grade was further analyzed by Evans Analytical Group  
 81 and is provided in Table 1.

82  
 83 Table 1. Chemical composition of the 316L grade stainless alloy.

Element	Wt. %	Element	Wt. %	Element	Wt. %	Element	Wt. %
Fe	Balance (~68)	Mn	1.3	N	0.08	C	0.017
Cr	16.9	Cu	0.6	V	0.06	Nb	0.007
Ni	10.5	Si	0.3	S	0.023	O	0.005
Mo	2.1	Co	0.1	P	0.02	H, B, Ti	<0.001

#### 85 3.2 Electron-beam welding

86 E-beam welding was used in this study since it is a low heat-input joining technique that results in  
 87 acceptable fusion zone and heat-affected zone (HAZ) properties such as the microstructure, weld purity,  
 88 and size of the weld/HAZ allowing to be fit in the gage section of 25.4 mm long SS-3 type miniature  
 89 tensile specimens. E-beam welding was performed using two metal weld blocks (thickness = 6.35 mm) of  
 90 the as-received 316L materials (Figure 1) clamped to a water-cooled chill block in an inert argon gas  
 91 glove box. The resulting weld blocks allowed to prepare tensile specimens in both parallel and  
 92 perpendicular to the texture direction of the base metal (discussed under Figure 2a). More details of the  
 93 welding procedure can be found elsewhere.<sup>14</sup>



97  
 98 Figure 1. (a) The as-received 316L material and (b) a sample of 316L welded using e-beam welding. RD  
 99 represents the rolling direction of the as-received material. A tensile bar with close to typical dimensions  
 100 of a SS-3 type specimen is also drawn on the welded block.  
 101

### 102 3.3 Tensile test bars

103 Tensile specimens of SS-3 type were cut by wire electro-discharge machining (EDM). To acquire a  
 104 smooth surface and to remove any surface oxide layers introduced by welding and EDM cutting, a similar  
 105 tensile specimen surface polishing and etching process described elsewhere was used.<sup>15</sup> That is, a  
 106 minimum of 32 finish (0.8 μm) surface roughness was obtained for the tensile bars using mechanical  
 107 polishing followed by EDM. Any deeper specimen surface defects (or any unwanted surface oxides)  
 108 introduced by mechanical polishing were removed by chemically etching (49 vol.% HNO<sub>3</sub>+2% HF) the  
 109 surface to remove 10 – 20 μm surface layer.

110 Tensile specimens of the as-received base metal were cut longitudinally and transversely with respect  
 111 to the RD of the as-received 316L blocks. Tensile specimens of the welded samples were cut longitudinal  
 112 or parallel to the RD to the welded base metal blocks and normal to the welding direction. The gage  
 113 sections of the tensile specimens included the weld, HAZ, and base metal as depicted pictorially in Figure  
 114 1. The width and length of the gage section of SS-3 tensile bars are 1.52 mm and 7.62 mm, respectively.

115 From this point onward, BML, BMT, and EBL will be used to indicate the three sets of SS-3 tensile  
 116 specimens, longitudinally cut base metal, transversely cut base metal, and longitudinally cut e-beam  
 117 welded samples, respectively.

### 118 3.4 Neutron irradiation

119 The three sets of SS-3 tensile specimens, BML, BMT, and EBL, were neutron irradiated at the High  
 120 Flux Isotope Reactor (HFIR) at Oak Ridge National laboratory (ORNL) using a specially designed  
 121 capsule to hold the samples. Two neutron fluences,  $1.37 \times 10^{18}$  and  $1.40 \times 10^{19}$  n/cm<sup>2</sup>,  $E > 0.1$  MeV at a  
 122 targeted irradiation temperature of 60–100 °C corresponding to  $1.1 \times 10^{-3}$  and  $1.1 \times 10^{-2}$  dpa (displacement  
 123 per atom), respectively were used.  
 124

125 3.5 Tensile testing

126 All the tensile testing of nonirradiated samples were performed using either an Instron 1125 or Instron  
127 4507 at room temperature. A 1,124 lb. load cell and a crosshead control at a strain rate of  $1 \times 10^{-3} \text{ s}^{-1}$  were  
128 used. The irradiated samples were tested using an Instron Model-1123 with an S-type load cell of 1000 lb.  
129 interface SM-1000 cell at the Irradiated Materials Examination and Testing (IMET) hot cell facility at  
130 ORNL. Ultimate tensile strength (UTS) or tensile strength (TS), yield strength (YS), uniform elongation  
131 (UE), which is equal to strain-to-necking (STN) of the samples tested in this current study, and total  
132 elongation (TE) were used to analyze the samples' tensile properties. Engineering stress/strain plots were  
133 also used for further characterization of the samples.

135 3.6 Microstructural characterization

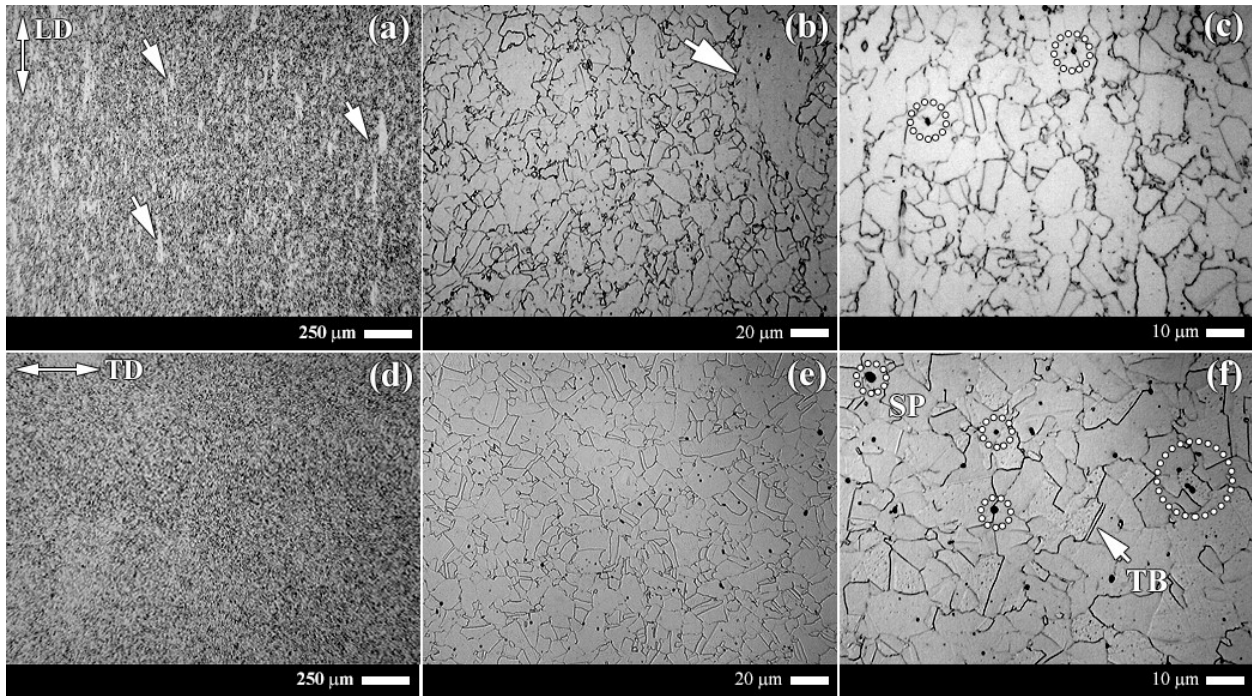
136 Microstructural characterization of the samples, both cross-sectional and fracture surface  
137 (fractography) was performed using optical microscopy (OM) and scanning electron microscopy (SEM).  
138 A Leica DMI5000 M optical microscopy and a Hitachi S-4700 cold field emission SEM and a JEOL 6500  
139 FEG-SEM were utilized. Energy dispersive spectroscopy (EDS) was also used for elemental mapping and  
140 point or line scans. Bright field imaging was used in OM. Both secondary electron (SE) and backscattered  
141 electron (BSE) modes were used with SEM imaging.

143 4. Results and discussion

144 4.1 Microstructure of 316L type stainless steel in its base metal and e-beam welded conditions

145 Stainless steel 316L grade sample showed a microstructure consisting of randomly distributed  
146 equiaxed grains (Figure 2). The sample cut longitudinal direction of the as-received 316L material  
147 showed some elongated grains characteristic of rolling the material during its production (Figure 2a). In  
148 other words, a texture can be present along the RD improving the tensile ductility of the specimen cut  
149 along this direction. This is why RD was used as a reference direction when cutting tensile specimens as  
150 discussed in section 3.3. However, the transversely cut sample did not have such character (Figure 2d).  
151 The BMT sample showed a significant amount of dark-contrast inclusions (Figure 2e-f), which can also  
152 be observed in BML sample (Figure 2b-c) but at a comparatively smaller concentration.

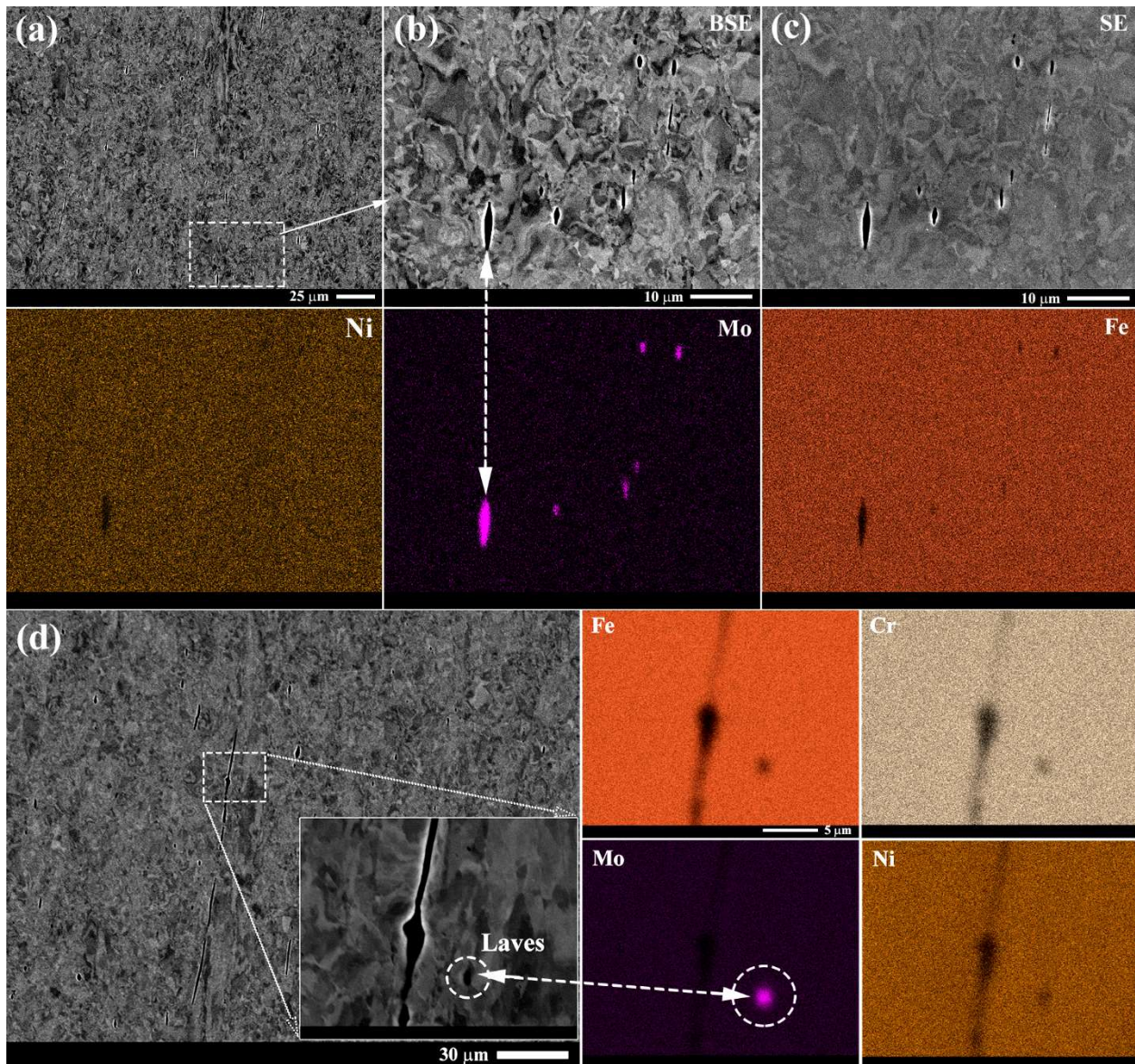
153



154

155 Figure 2. OM images of two surfaces of the as-received 316L base metal material: (a-c) BML and (d-f)  
 156 BMT. TD and LD represent transverse and longitudinal directions with respect to the RD of the as-  
 157 received material, respectively. Few secondary precipitates (SP) and twin boundary (TB) are also  
 158 highlighted.  
 159

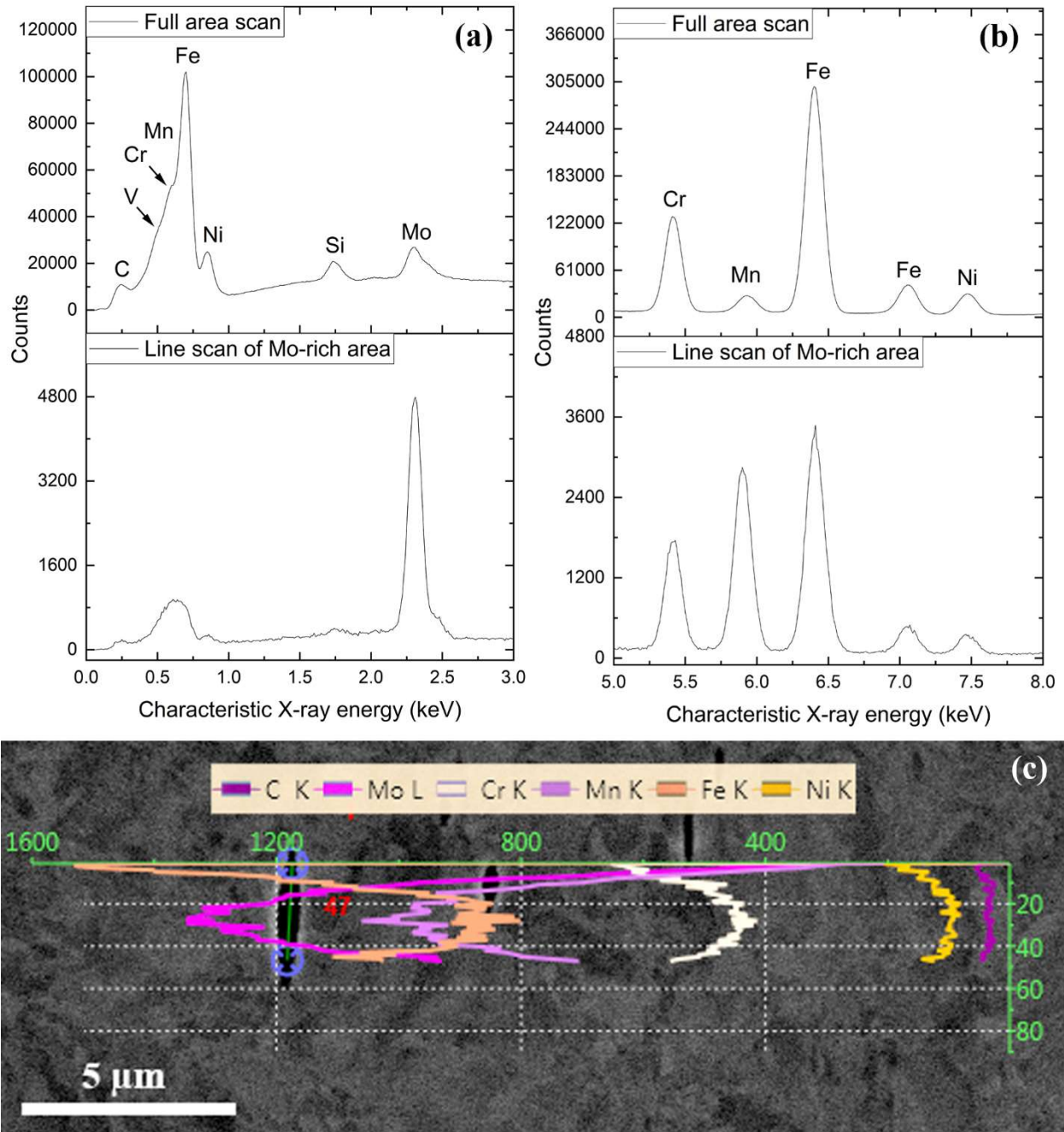
160 The as-received 316L base metal sample showed somewhat deformed microstructure that usually  
 161 observed in cold-worked materials (Figure 3).<sup>16</sup> This surface feature is more pronounced in the high-  
 162 resolution images as depicted in Figure 3b-d. As can be observed in Figure 3, sample consisted of dark  
 163 contrast areas some of which are narrow voids (Figure 3b-c) and are minor precipitates (Figure 3d). Also,  
 164 the voids or precipitates are rich with Mo as shown in the EDS elemental maps of the corresponding areas  
 165 as a result of ~2 wt. % Mo in 316L samples.  
 166



167  
 168 Figure 3. SEM imaging and EDS elemental maps of two areas of 316L SS base metal sample. (a) BSE  
 169 SEM image at a low resolution and (b) at a high resolution. (c) The SE SEM image of (b). EDS elemental  
 170 maps of the area in (b) are also shown; only Ni, Mo, and Fe maps are shown. (d) Low resolution BSE  
 171 SEM image of another area with a high-resolution image of the highlighted location in the inset. EDS  
 172 elemental maps of that area are shown at the bottom right side.  
 173

174 The EDS spectra (Figure 4a, b) of the area depicted in Figure 3b show the presence of the elements  
 175 expected in the 316L SS base metal identified by elemental analysis (Table 1). Mo and Mn were also  
 176 observed in this sample area and their concentrations were high in the area identified as Mo-rich (Mo map  
 177 in Figure 3) as is shown in the line scan in Figure 4c. Although the relative peak intensities of Fe, Cr, and  
 178 Ni are low but not zero in the Mo-rich area, these line scan data, especially of Mo and Mn, indicate the

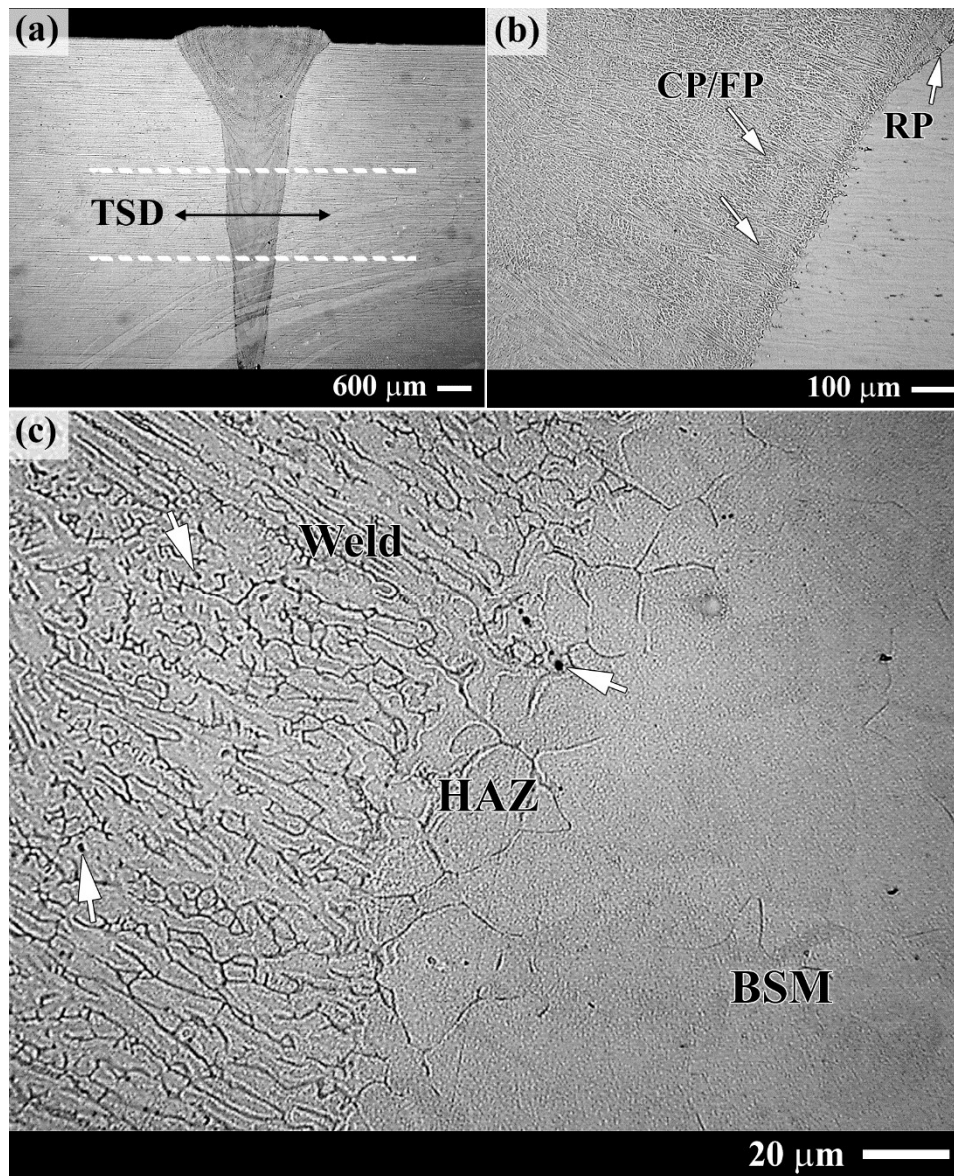
179 presence of intermetallic or Laves phase characteristics that can be commonly observed at this scale using  
 180 SEM imaging.<sup>17</sup>  
 181



182  
 183 Figure 4. EDS spectra (area shown in Figure 3b) and a line scan of Mo-rich area (highlighted in in Figure  
 184 3b) and the SEM micrograph of 316L SS base metal sample. EDS spectra in (a) 0 – 3.0 keV and (b) 5.0 –  
 185 8.0 keV ranges. (c) Line scan and the SEM micrograph.

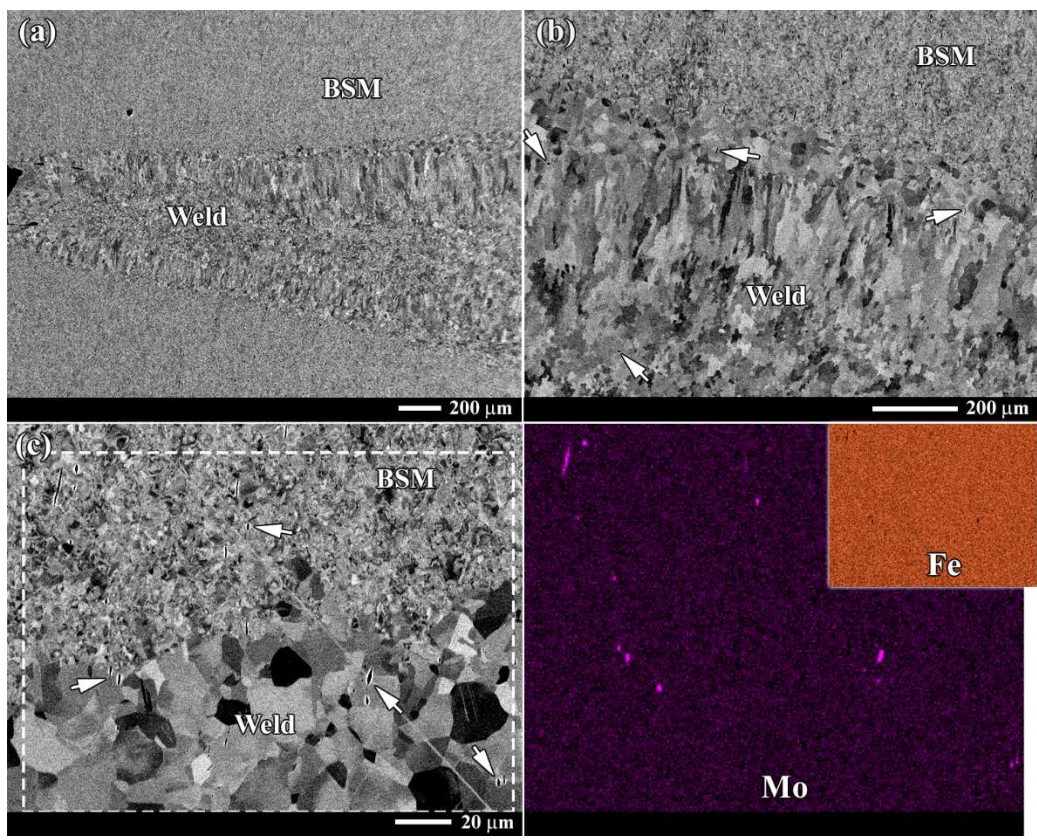
186

187 Optical micrographs of the as e-beam welded (not tensile specimens) 316L showed narrow weld zone  
 188 (Figure 5a-b) with seamless HAZ, which consists of microstructures similar to full penetration weld close  
 189 to the fusion zone and partial penetration weld in the base metal side (Figure 5c). As highlighted in Figure  
 190 5b, different welding passes, including the root pass edge, can also be identified from these OM images.  
 191 As in the case of base metal, weld pool also consisted of dark contrast inclusions as highlighted by arrows  
 192 in Figure 5c. The grains in the weld also surrounded by dark contrast grain boundaries (GB) due to  
 193 greater level of etching of GB ferrite phase, which usually forms during welding.<sup>9, 18</sup>  
 194



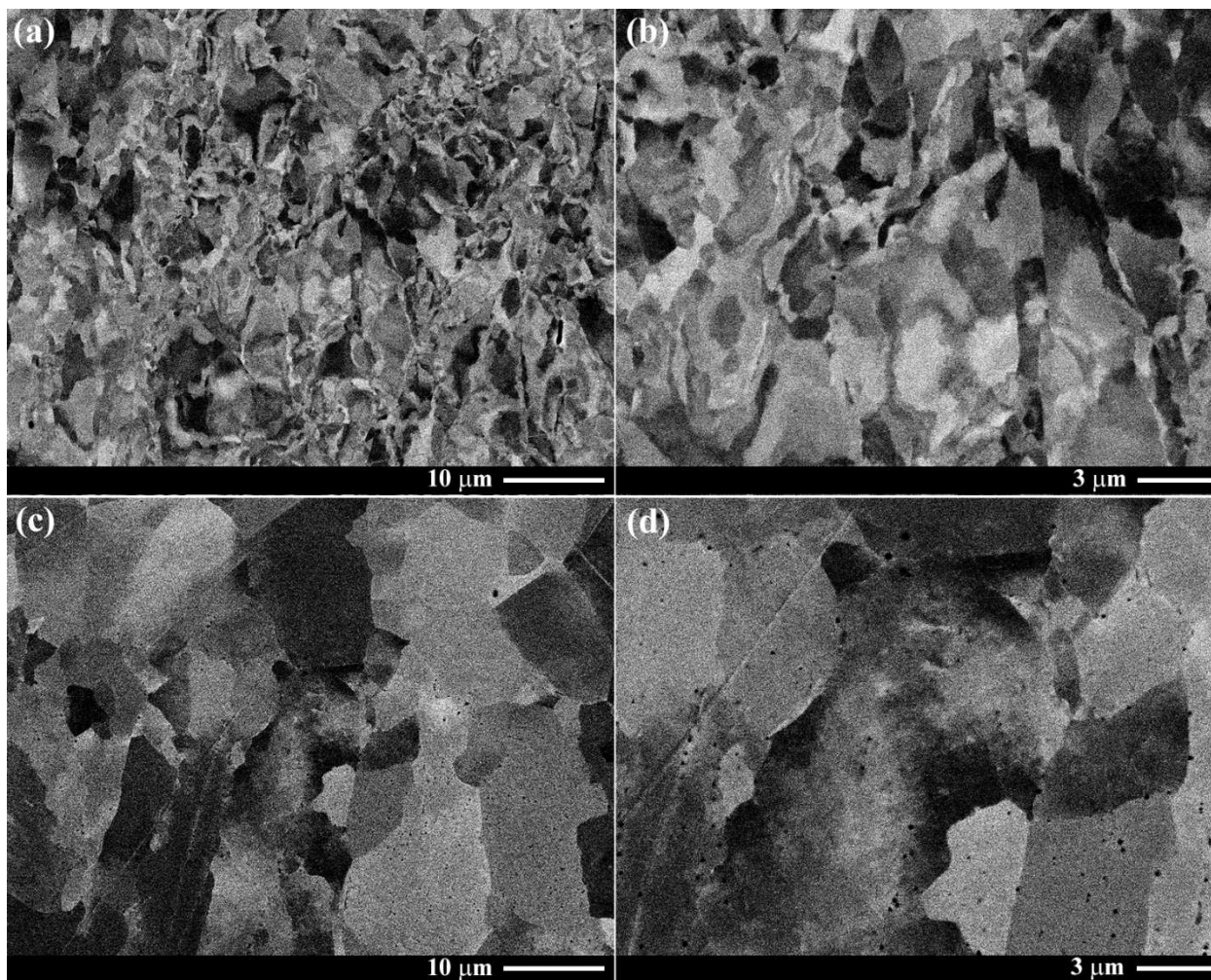
195  
 196 Figure 5. OM images of e-beam welded 316L SS block sample: (a) an area with weld pool and the tensile  
 197 strain direction (TSD) in which tensile testing was conducted, (b) a side view highlighting edges of root  
 198 pass (RP), cover pass (CP), and final pass (FP), and (c) a high-resolution image.  
 199

200 Microstructures of base metal and weld/HAZ areas of an e-beam welded 316L SS sample imaged  
201 using SEM are shown in Figure 6. As it is apparent in Figure 6-a, well grown and resolved grains can be  
202 observed in the weld pool compared to the base metal area of the sample, even at low resolution.  
203 However, the grains are smaller at the center of the weld pool. Most of the weld pool grains show angular  
204 and elongated shape (Figure 6b), while some areas contain more rounded or equiaxed grains (Figure 6c).  
205 Identification of HAZ is difficult with SEM imaging. The dark contrast areas correspond to the Mo-rich  
206 precipitates are also observed in the SEM micrographs of the base metal and weld pool areas as were  
207 confirmed using EDS elemental maps. These micro-sized Mo-rich areas also do not have any apparent  
208 relationship with GBs of the large and well-formed grains in the fusion zone. Also, the columnar laths are  
209 mostly directional to the RD of the base metal areas as was observed in the control samples, which  
210 probably indicates that the presence of the Mo-rich precipitates in the weld zone were just a reformation  
211 and not caused by welding.  
212



213  
214 Figure 6. BSE SEM micrographs of an e-beam welded 316L SS block sample at (a) low and (b) high  
215 resolution modes. EDS maps of the weld-base metal area highlighted in (c) are shown to the right side in  
216 the figure; only Mo and Fe maps are shown.  
217

218 Furthermore, high resolution SEM imaging showed that the e-beam welded samples contain finer  
219 inclusions (<1  $\mu\text{m}$  size) or pores along GBs and within austenite grains in the weld (Figure 7c-d) as  
220 compared to the base metal regions (Figure 7a-b). This could imply that the weld pool might have more  
221 and finer secondary precipitates than in the base metal areas.  
222



223  
224 Figure 7. BSE SEM images of base metal (a-b) and weld pool (c-d) of e-beam welded 316L SS block  
225 sample at two different resolutions.  
226

#### 227 4.2 Irradiation behavior of 316L-grade stainless steel samples

228 Nonirradiated base metal samples cut longitudinally or parallel to the RD of 316L SS materials  
229 showed mechanical strength in the order of  $\sim 700$  MPa and total elongation in  $\sim 70\%$  (Table 2). Compared  
230 to the longitudinally cut sample,  $\sim 10\%$  lower TE is observed in the nonirradiated BSM sample cut along  
231 the transverse direction to the RD of 316L materials, while no significant change in the mechanical  
232 strength is present. Compared to the longitudinally cut base metal sample, a slight decrease in mechanical

233 strength and close to 50% lower TE value in the nonirradiated e-beam welded sample were observed. An  
 234 increase in both UTS and YS with the increase in fluence values is present in the samples. TE decreased  
 235 with the increase in fluence values in all the samples, while it is lowest in the e-beam welded samples for  
 236 all conditions. A closely similar behavior can be observed in the UE values of the samples.

237  
 238 Table 2. Tensile properties of 316L type SS samples. Standard deviation of UTS and YS varied in 3–74  
 239 MPa range and UE and TE varied in 2–7% range. RI and RiD indicate relative increase and decrease with  
 240 respect to the nonirradiated sample of each sample type. Standard deviation of the data are given inside  
 241 brackets.

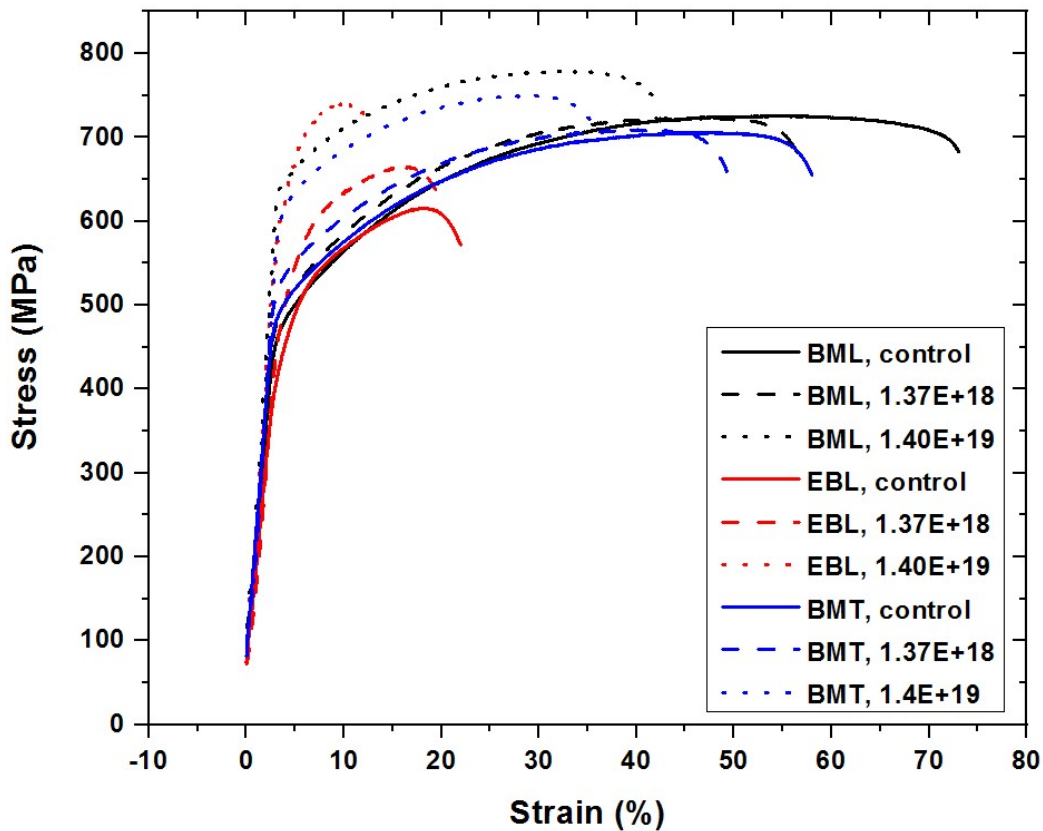
Sample type and the irradiation (fluence; n/cm <sup>2</sup> , E>0.1 MeV)	UTS (MPa)	RI (%)	YS (MPa)	RI (%)	UE (%)	RiD (%)	TE (%)	RiD (%)
BML, 0	726 (2)		444 (3)		55 (4)		77 (4)	
BML, 1.37E+18	724 (1)	<1	462 (14)	4	41 (1)	25	58 (1)	25
BML, 1.40E+19	779 (1)	7	629 (3)	42	29 (1)	47	44 (1)	43
BMT, 0	706 (56)		468 (8)		48 (3)		64 (3)	
BMT, 1.37E+18	711 (3)	<1	511 (14)	9	35 (2)	27	45 (3)	30
BMT, 1.40E+19	761 (7)	8	654 (37)	40	21 (4)	56	32 (1)	50
EBL, 0	621 (5)		405 (7)		18 (2)		28 (2)	
EBL, 1.37E+18	666 (1)	7	460 (28)	14	12 (1)	33	21 (1)	25
EBL, 1.40E+19	740 (1)	19	549 (1)	36	6 (1)	67	16 (1)	43

242  
 243  
 244 As shown Figure 8, 316L SS base metal sample cut parallel to the RD showed highest tensile ductility  
 245 and greatest strain hardening. With the increase in neutron fluence, these samples start to decrease their  
 246 tensile ductility and the amount of strain hardening. The samples also decrease the ability to strain  
 247 plastically in a similar manner. The overall increase in the engineering TS and YS of the post-irradiated  
 248 BM samples also show radiation-induced hardening. The relative increase in YS of the BM samples (cut  
 249 both along longitudinal and transverse directions) increase from 4 – 9% to 40 – 42% (Table 2) when the  
 250 fluence values increase from  $1.37 \times 10^{18}$  to  $1.40 \times 10^{19}$  n/cm<sup>2</sup> even at 60–100 °C irradiation temperature.  
 251 This indicates that while radiation-induced hardening is present in the BM samples for both irradiation  
 252 conditions, it increases with the increase in the irradiation dose from 0.001 to 0.01 dpa (fluence from  
 253  $1.37 \times 10^{18}$  to  $1.40 \times 10^{19}$  n/cm<sup>2</sup>). A similar behavior of tensile properties of 316LN, which has higher Ni  
 254 and lower Cr levels than in 316L, samples that were proton irradiated at 64 – 164 °C is reported by  
 255 Farrell.<sup>19</sup> They have shown loss of ductility and considerable irradiation hardening in 316LN samples  
 256 with the increase in dose. Other studies also reported an increase in irradiation hardening of 316L samples  
 257 with the increase in dose. These studies include neutron irradiation to dose values of 0.5 dpa at 227 °C,<sup>20</sup>  
 258 krypton ion irradiation up to 3 dpa at 350 °C,<sup>21</sup> neutron irradiated fuel cladding with doses of 0 – 80 dpa  
 259 at 430 – 500 °C,<sup>22</sup> xenon ion irradiation up to 3.7 dpa at room temperature and 350 °C,<sup>23</sup> and neutron  
 260 irradiation up to 2 dpa at 300 – 600 °C<sup>24</sup> etc. In the case of longitudinally cut e-beam welded samples,  
 261 lowest tensile ductility among all samples and a decrease in its TE with the increase in fluence can be

262 observed. Increases in TS and YS, as well as radiation hardening of the irradiated e-beam welded samples  
263 are apparent in their stress-strain curves. The larger overall relative increases in TS and YS of the welded  
264 samples also indicate that the welded samples have the greatest radiation hardening among the samples  
265 tested here. The strain hardening is minimum in the e-beam welded sample irradiated at  $1.40 \times 10^{19}$  n/cm<sup>2</sup>  
266 ( $E > 0.1$  MeV).

267 No radiation softening was observed in any of these samples since they were irradiated at lower  
268 fluences and/or lower temperatures than in other studies that reported such behavior in austenite steels.<sup>5,</sup>  
269 12, 25, 26

270



271

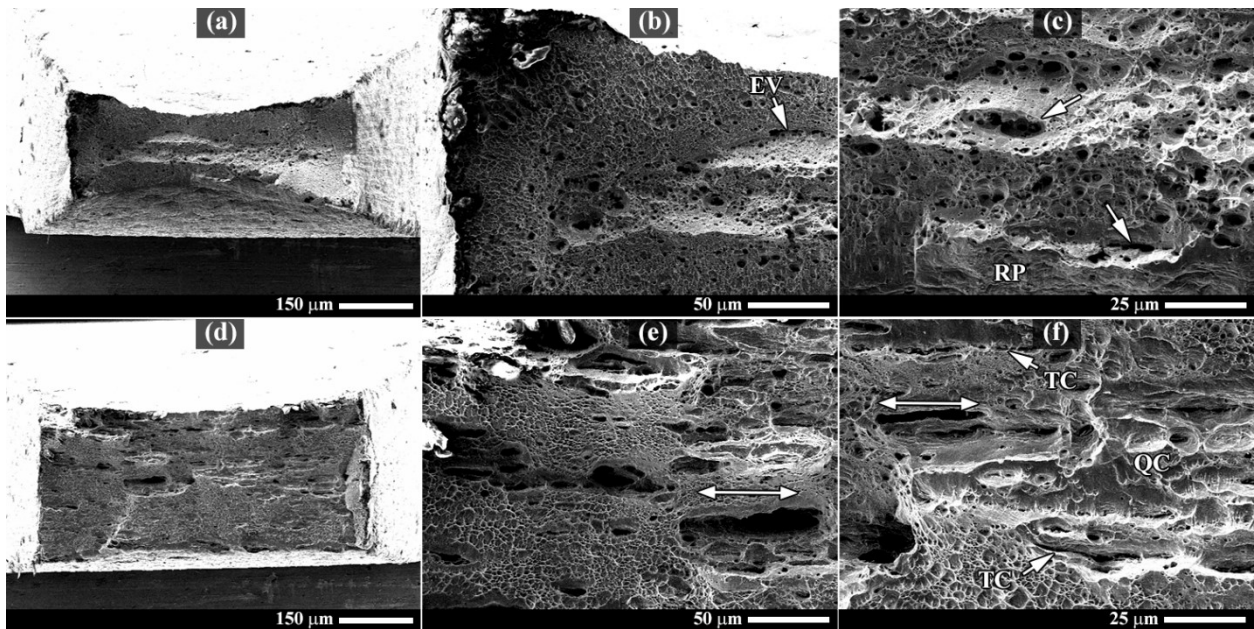
272 Figure 8. Engineering stress vs. strain plots of 316L type SS samples as a function of irradiation  
273 conditions.  
274

275 As discussed above, 316L base metal tensile specimens cut longitudinal to the RD showed the  
276 greatest amount of tensile ductility at its nonirradiated condition. It also had considerable amount of  
277 necking, which was further confirmed by the fracture surface of the sample depicted in Figure 9a. This  
278 sample showed microvoid coalescence ductile fracture with characteristic dimples or cup-like depressions  
279 at different sizes. Inhomogeneous fracture or shearing and few elongated voids (highlighted by arrows in  
280 Figure 9b-c) can also be observed in this fracture surface. Some shearing river patterns observed at the

281 fracture surface edge furthermore indicates the earlier shearing prior to the further tensile deformation and  
282 necking.

283 The fracture surface of the transversely cut nonirradiated 316L base metal sample (Figure 9d) also  
284 showed that it had some necking, but at slightly lower amount compared to the longitudinally cut sample  
285 (the differences in TE and UE in longitudinal and transversely cut base metal samples are 22 and 16%,  
286 respectively). This sample also showed a ductile rupture with a fracture surface dominated by a dimple  
287 structure. Some areas in the fracture surface also consisted of cracks that can be identified as  
288 transgranular type, which usually means high ductility. However, a significant amount of voids elongated  
289 along the direction transverse to the tensile deformation direction could be observed (Figure 9d-f). A few  
290 isolated areas featuring quasi-cleavage type structure can also be observed as highlighted in Figure 9f.  
291 These observations indicate that the nature of the ductile rupture in transversely cut sample is lower than  
292 that of the longitudinally cut 316L SS base metal samples even in their nonirradiated condition.

293

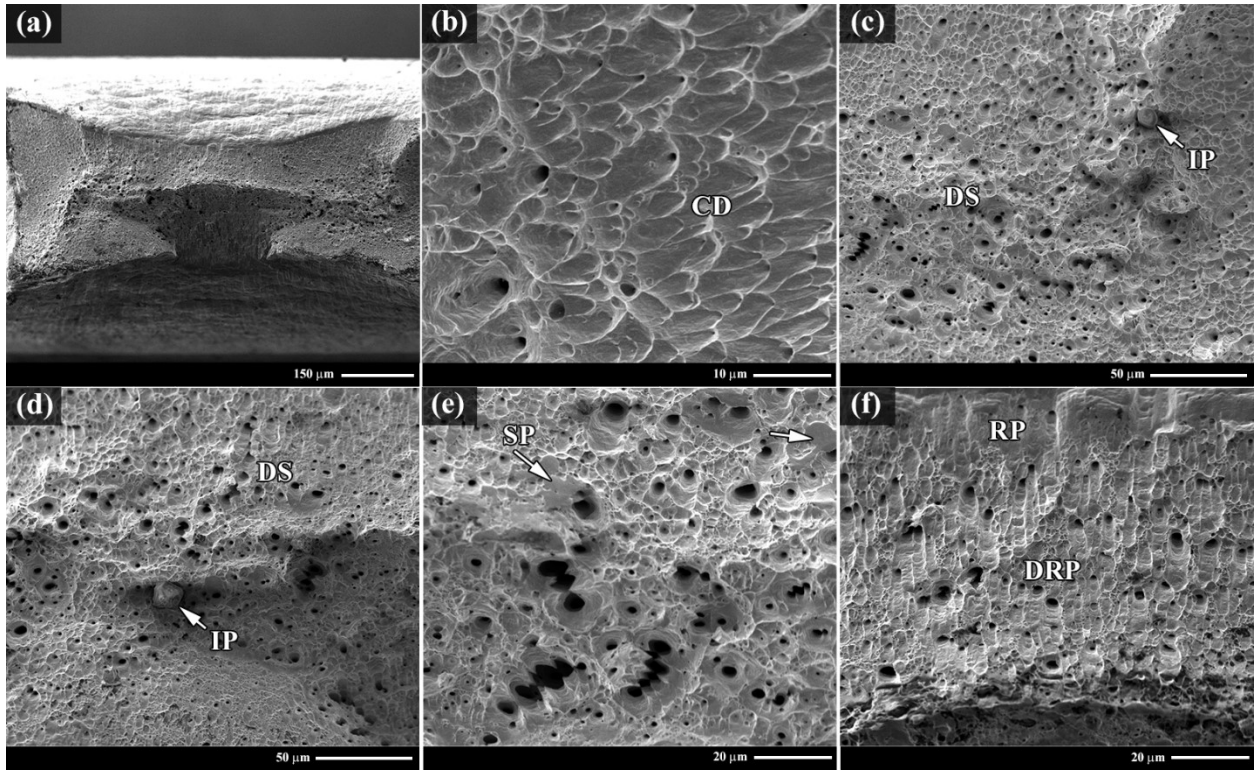


294

295 Figure 9. SEM micrographs of fracture surfaces of BML (a-c) and BMT (d-f) 316L SS samples. EV, RP,  
296 TC, and QC denote elongated voids, river patterns, transgranular cracks, and quasi-cleavages,  
297 respectively.  
298

299 The neutron irradiated ( $1.40 \times 10^{19}$  n/cm<sup>2</sup>) longitudinally cut base metal samples mostly showed  
300 fracture surface features characteristic of ductile rupture, which is generally observed in irradiated 316L  
301 type austenite steels.<sup>27</sup> These include cup-like depressions (Figure 10b) and linked microvoids (Figure  
302 10c) with some necking features (Figure 10a). Some inclusions, elongated voids, and some isolated shear  
303 patches can also be observed in this sample (Figure 10c-e). The inclusions could be an  $\sigma$  phase or Laves

304 phase precipitation. While dimple structure is present in the fracture surface area corresponding to  
 305 necking, these microvoids are linked with river patterns that propagate in a direction normal to the tensile  
 306 deformation direction. Shearing with river pattern but lacking dimple structure can also be observed just  
 307 above this area (Figure 10f). These features indicate radiation hardening and lower ductility of the post-  
 308 irradiated BM samples compared to the pre-irradiated samples.  
 309

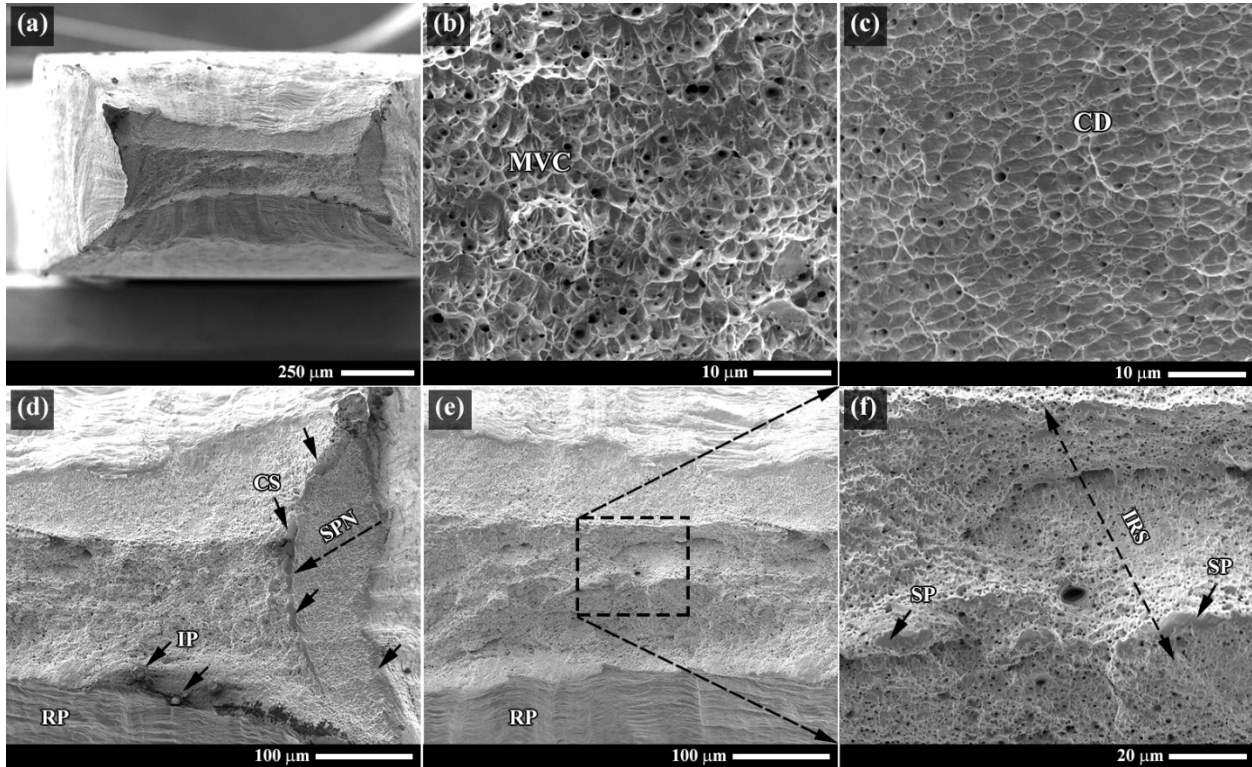


310  
 311 Figure 10. SEM micrographs of the fracture surface of BML sample irradiated at  $1.40 \times 10^{19} \text{ n/cm}^2$  ( $E > 0.1$   
 312 MeV). (a) The overall fractography, (b-e) a few different areas with different fracture surface features,  
 313 and (f) an area just above the necking feature. CD, DS, IP, SP, RP, and DRP denotes cup-like  
 314 depressions, dimple structure, isolated precipitates, shear patches, river patterns, and dimple coalesced  
 315 with river patterns.  
 316

317 Contrary to the significantly low TE values, the fractography of the neutron irradiated ( $1.40 \times 10^{19}$   
 318  $\text{n/cm}^2$ ) longitudinally cut e-beam welded sample (Figure 11) showed similar properties to those of the  
 319 post-irradiated base metal samples (Figure 10). However, a couple of differences such as the presence of  
 320 layered shear patches at one edge of the surface (Figure 11d) and some inhomogeneous rupture probably  
 321 due to shear patches within the fracture surface (Figure 11e-f) can be observed. These two things mostly  
 322 present in the irradiated e-beam welded sample might indicate a slight increase in irradiation hardening  
 323 and the corresponding decrease of tensile ductility. Although no significant amount of transgranular  
 324 fracture was observed in both base metal and e-beam welded irradiated samples, lower amount of

325 elongation of voids was identified in the e-beam welded sample in the post-irradiated condition inferring  
 326 the fracture occurred mostly via intergranularly lowering ductility of the e-beam welded samples. <sup>28</sup>  
 327 Closely similar microstructure of the fracture surface of post-irradiated e-beam welded samples to that of  
 328 the base metal samples also indicate the presence of some tensile ductility in the post-irradiated welded  
 329 samples as is shown by their TE values (16 – 21%). It is also possible that the tensile fracture occurred  
 330 either near the HAZ/BM boundary or in the HAZ since the lowest TE values observed in the e-beam  
 331 welded as was observed by Horste. <sup>5</sup>

332



333

334 Figure 11. Fracture surface SEM micrographs of EBL sample irradiated up to  $1.40 \times 10^{19} \text{ n/cm}^2$ . (a-f)  
 335 Show different fracture surface properties of a few different areas with MVC, RP, IP, CS, SPN  
 336 highlights that denote micro-void coalescence, river patterns, isolated precipitates, continuous shearing,  
 337 shear patch network, and inhomogeneous rupture due to shearing, respectively.  
 338

339

340 Conclusions

341 Effects of low-temperature (60–100 °C) neutron irradiations, up to  $1.40 \times 10^{19} \text{ n/cm}^2$  ( $E > 0.1 \text{ MeV}$ ), on  
 342 the tensile behavior of 316L type SS was studied. Three sets of samples (two base metal and one e-beam  
 343 welded) were irradiated. The 2.1 wt. % Mo containing austenite SS base metal material and the e-beam  
 344 welded samples showed to contain secondary precipitates rich with Mo. The e-beam welded samples

345 showed the presence of duplex type two-phased fusion zone, which was identified as austenite grains with  
346 ferrite grain boundaries and a seamless HAZ.

347 While highest TE was observed in the base metal samples cut parallel to the RD of the as-received  
348 316L blocks, lowest TE values were observed in the e-beam welded samples. The low-temperature  
349 neutron irradiation decreased the TE of all the samples, while increasing their UTS and YS. Radiation-  
350 induced hardening was also observed in the samples and was increased with the increase in neutron  
351 fluences on them. Fracture surfaces of the samples showed that all the samples, pre- and post-irradiated,  
352 consist of ductile features mostly. While some transgranular fracturing was observed in the pre-irradiated  
353 samples, mostly intergranular fracturing was observed in the post-irradiated samples indicating a  
354 corresponding decrease in the tensile ductility. Also, features such as isolated inclusions, shear patches,  
355 and some river patterns sometimes mixed with dimples were identified in the ruptured irradiated sample  
356 surfaces. Frequency of shear patches were greater in the e-beam welded irradiated samples than in the  
357 base metal samples. Networks of shear patches were also observed at fracture surface edges of the e-beam  
358 welded irradiated samples. Shearing-dominated inhomogeneous rupture was also greater in the irradiated  
359 e-beam welded samples.

360

#### 361 Acknowledgements

362 Funding for this research work was provided by the US Department of Energy's National Nuclear  
363 Security Administration (DOE/NNSA), Office of Material Management and Minimization's  
364 Molybdenum-99 Program. The authors would also like to thank their coworkers at ORNL for their  
365 support in this research work: Tom Geer, Christopher Stevens, Michael McAlister, Maxim Gussev, Pat  
366 Bishop, and Joel McDuffee. This work was also performed under the auspices of the U.S. Department of  
367 Energy (DOE) by Lawrence Livermore National Laboratory (LLNL) under Contract No. DE-AC52-  
368 07NA27344.

369

370

371 Conflict of Interest Statement

372 On behalf of all authors, the corresponding author states that there is no conflict of interest.

373

374

375 REFERENCES

- 
- <sup>1</sup> A. S. Lima, A. M. Nascimento, H. F. G. Abreu, P. De Lima-Neto, *J. Mater. Sci.* 2005, vol. 40, pp. 139-144.
- <sup>2</sup> E. A. Kenik, J. T. Busby, *Mater. Sci. Eng. R*, 2012, vol. 73, pp. 67-83.
- <sup>3</sup> H. R. Brager, F. A. Garner, *J. Nucl. Mater.*, 1978, vol. 73, pp. 9-19.
- <sup>4</sup> P. J. Maziasz, *J. Nucl. Mater.*, 1982, vol. 108-109, pp. 359-384.
- <sup>5</sup> M. G. Horsten, M. I. de Vries, *J. Nucl. Mater.*, 1994, vol. 212-215, pp. 514-518.
- <sup>6</sup> J. L. Scott, M. L. Grossbeck, A. Hishinuma, T. Kondo, A. F. Rowcliffe, M. P. Tanaka, *J. Nucl. Mater.*, 1986, vol. 141-143, pp. 996.
- <sup>7</sup> S. Saito, K. Fukaya, S. Ishiyama, H. Amezawa, M. Yonekawa, F. Takada, Y. Kato, T. Takeda, H. Takahashi, M. Nakahira, *J. Nucl. Mater.*, 2002, vol. 307-311, pp. 1573-1577.
- <sup>8</sup> T. Bulanova, A. Fedoseev, G. Kalinin, B. Rodchenkov, V. Shamardin, *J. Nucl. Mater.*, 2004, vol. 329-333, pp. 639-642.
- <sup>9</sup> K. Farrell, T. S. Byun, *J. Nucl. Mater.*, 2006, vol. 356, pp. 178-188.
- <sup>10</sup> M. N. Babu, B. S. Dutt, S. Venugopal, G. Sasikala, S. K. Albert, A. K. Bhaduri, T. Jayakumar, *Procedia Eng.*, 2013, vol. 55, pp. 716-721.
- <sup>11</sup> A. K. Suri, N. Krishnamurthy, I. S. Batra, *J. Phys.: Conf. Ser.*, 2010, vol. 208, pp. 012001.
- <sup>12</sup> J. D. Elen, P. Fenici, *J. Nucl. Mater.*, 1992, vol. 191-194, pp. 766-770.
- <sup>13</sup> SHINE Medical technologies, 2020, Demonstrated technology, June, 2020, (<https://shinemed.com/demonstrated-technology/>)
- <sup>14</sup> C. Silva, K. Leonard, L. Garrison, C. Bryan, *Mater. Sci. Eng. A*, 2021, vol. 823, pp. 141780.
- <sup>15</sup> C. Silva, K. Leonard, M. Trammel, C. Bryan, *Mater. Sci. Eng. A*, 2018, vol. 716, pp. 296-307.
- <sup>16</sup> C. Silva, M. Song, K. Leonard, M. Wang, G. Was, J. Busby, *Mater. Sci. Eng. A*, 2017, vol. 691, pp. 195-202.
- <sup>17</sup> T. Rahman, W. L. Ebert, J. E. Indacochea, *Corrosion Engineering, Science and Technology; The International Journal of Corrosion Processes and Corrosion Control*, 2018, vol. 53, pp. 226-223.
- <sup>18</sup> S. A. David, J. M. Vitek, R. W. Reed, T. L. Hebble, Report No. ORNL/TM-10487, ORNL, 1987.
- <sup>19</sup> K. Farrell, T. S. Byun, *J. Nucl. Mater.*, 2001, vol. 296, pp. 129-138.
- <sup>20</sup> M.I. de Vries, in: J.G. Van der Laan (Ed.), ECN (Petten) Rept. ECN-C-90-041, 1990, p. 66
- <sup>21</sup> C. Robertson, L. Boulanger, S. Poissonnet, *J. Nucl. Mater.*, 1999, vol. 217&272, pp. 102-105.
- <sup>22</sup> V. Karthik, S. Murugan, P. Parameswaran, C. N. Venkiteswaran, K. A. Gopal, N. G. Muralidharan, S. Saroja, K.V. Kasiviswanathan, *Energy Procedia*, 2011, vol. 7, pp. 257-263.
- <sup>23</sup> J. Lin, F. Chen, X. Tang, J. Liu, S. Shen, G. Ge, *Vacuum*, 2020, vol. 174, pp. 109183.
- <sup>24</sup> T. S. Byun, B. E. Garrison, M. R. McAlister, X. Chen, M. N. Gussev, T. G. Lach, A. Le Coq, K. Linton, C. B. Joslin, J. K. Carver, F. A. List, R. R. Dehoff, K. A. Terrani, *J. Nucl. Mater.*, 2021, vol. 548, pp. 152849.
- <sup>25</sup> M. P. Tanaka, S. Hamada, A. Hishinuma, M. L. Grossbeck, *J. Nucl. Mater.* 1988, vol. 155-157, pp. 957.
- <sup>26</sup> S. A. Maloy, M. R. James, W. R. Johnson, T. S. Byun, K. Farrell, M. B. Toloczko, *J. Nucl. Mater.*, 2003, vol. 318, pp. 283-291.
- <sup>27</sup> E. Stergar, S. G. Eremin, S. Gavrilov, M. Lambrecht, O. Makarov, V. Iakovlev, *J. Nucl. Mater.*, 2016, vol. 473, pp. 28-34.
- <sup>28</sup> W.R. Martin, J.R. Weir, Report No. ORNL-TM-1005, ORNL, 1965.